A *HUBBLE* DIAGRAM FROM TYPE II SUPERNOVAE BASED SOLELY ON PHOTOMETRY: THE PHOTOMETRIC COLOR METHOD[*]

T. DE JAEGER[1,2], S. GONZÁLEZ-GAITÁN[1,2], J. P. ANDERSON[3], L. GALBANY[1,2], M. HAMUY[1,2], M. M. PHILLIPS[4], M. D. STRITZINGER[5], C. P. GUTIÉRREZ[1,2,3], L. BOLT[6], C. R. BURNS[7], A. CAMPILLAY[4], S. CASTELLÓN[4], C. CONTRERAS[5], G. FOLATELLI[8,9], W. L. FREEDMAN[10], E. Y. HSIAO[4,5,11], K. KRISCIUNAS[12], W. KRZEMINSKI[13], H. KUNCARAYAKTI[1,2], N. MORRELL[4], F. OLIVARES E.[1,14], S. E. PERSSON[7], AND N. SUNTZEFF[12]

[1] Millennium Institute of Astrophysics, Santiago, Chile; dthomas@das.uchile.cl
[2] Departamento de Astronomía—Universidad de Chile, Camino el Observatorio 1515, Santiago, Chile
[3] European Southern Observatory, Alonso de Córdova 3107, Casilla 19, Santiago, Chile
[4] Las Campanas Observatory, Carnegie Observatories, Casilla 601, La Serena, Chile
[5] Department of Physics and Astronomy, Aarhus University, Ny Munkegade 120, DK-8000 Aarhus C, Denmark
[6] Argelander Institut für Astronomie, Universität Bonn, Auf dem Hgel 71, D-53111 Bonn, Germany
[7] Observatories of the Carnegie Institution for Science, Pasadena, CA 91101, USA
[8] Instituto de Astrofísica de La Plata, CONICET, Paseo del Bosque S/N, B1900FWA, La Plata, Argentina
[9] Institute for the Physics and Mathematics of the Universe(IPMU), University of Tokyo, 5-1-5 Kashiwanoha, Kashiwa,Chiba 277-8583, Japan
[10] Department of Astronomy and Astrophysics, University of Chicago, Chicago, IL 60637, USA
[11] Department of Physics, Florida State University, Tallahassee, FL 32306, USA
[12] George P. and Cynthia Woods Mitchell Institute for Fundamental Physics and Astronomy, Department of Physics and Astronomy, Texas A&M University, College Station, TX 77843, USA
[13] N. Copernicus Astronomical Center, ul. Bartycka 18, 00-716 Warszawa, Poland
[14] Departamento de Ciencias Fisicas—Universidad Andres Bello, Avda. República 252, Santiago, Chile

ABSTRACT

We present a Hubble diagram of SNe II using corrected magnitudes derived only from photometry, with no input of spectral information. We use a data set from the Carnegie Supernovae Project I for which optical and near-infrared light curves were obtained. The apparent magnitude is corrected by two observables, one corresponding to the slope of the plateau in the V band and the second a color term. We obtain a dispersion of 0.44 mag using a combination of the $(V - i)$ color and the r band and we are able to reduce the dispersion to 0.39 mag using our golden sample. A comparison of our photometric color method (PCM) with the standardized candle method (SCM) is also performed. The dispersion obtained for the SCM (which uses both photometric and spectroscopic information) is 0.29 mag, which compares with 0.43 mag from the PCM for the same SN sample. The construction of a photometric Hubble diagram is of high importance in the coming era of large photometric wide-field surveys, which will increase the detection rate of supernovae by orders of magnitude. Such numbers will prohibit spectroscopic follow up in the vast majority of cases, and hence methods must be deployed which can proceed using solely photometric data.

Key words: distance scale – galaxies: distances and redshifts – supernovae: general

1. INTRODUCTION

A fundamental probe in modern astronomy to understand the universe, its history, and evolution is the measurement of distances. Stellar parallax and the spectroscopic parallax allow us to reach ∼100–1000 pc, respectively, but farther afield other methods are needed. A traditional technique for measuring distances consists of applying the inverse square law for astrophysical sources with known absolute magnitudes, also known as standard candles. One of the first such objects used in astronomy was Cepheid stars. A Cepheid star's period is directly related to its intrinsic luminosity (Leavitt 1908; Benedict et al. 2007) and allows one to probe the universe to 15 Mpc. To attain larger distances, brighter objects are required. Type Ia supernovae (SNe Ia) have an absolute *B*-band magnitudes of about −19.5 to −19.2 mag (depending on the assumptions of H_0 Richardson et al. 2002; Riess et al. 2011)

which can be precisely calibrated using photometric and/or spectroscopic information from the SN itself, and can be used as excellent distance indicators. Indeed, there are two parameters correlated to the luminosity. The first one is the decline rate: SNe Ia with fast decline rates are fainter and have narrower light curve peaks (Phillips 1993), and the second one is color (Riess et al. 1996; Tripp 1998): redder SNe Ia are fainter. The standardization of SNe Ia to a level ∼0.15–0.2 mag (Phillips 1993; Hamuy et al. 1996; Riess et al. 1996) led to the measurement of the expansion history of the universe and showed that, contrary to expectations, the universe is under-going an accelerated expansion (Riess et al. 1998; Schmidt et al. 1998; Perlmutter et al. 1999). Within this new paradigm, one of the greatest challenges is the search for the mechanism that causes the acceleration, an endeavour that will require exquisitely precise measurements of the cosmological para-meters that characterize the current cosmological concordance model, i.e., ΛCDM model. Several techniques that offer the promise to provide such constraints have been put forward over recent years: refined versions of the SNe Ia method (Betoule et al. 2014), cosmic microwave background radiation measure-ments (Cosmic Microwave Background Explorer, Fixsen

et al. 1996; Jaffe et al. 2001; *Wilkinson Microwave Anisotropy Probe*, Bennett et al. 2003; Spergel et al. 2007; and more recently the Planck mission, Planck Collaboration et al. 2013), and baryon acoustic oscillation measurements (Blake & Glazebrook 2003; Seo & Eisenstein 2003). All of the above techniques have their own merits, but also their own systematic uncertainties that could become dominant with the increasingly higher level of precision required. Thus, it is important to develop as many methods as possible, since the truth will likely emerge from the combination of different independent approaches.

While SNe Ia have been used as the primary diagnostic in constraining cosmological parameters, type IIP supernovae (SNe IIP) have also been established to be useful independent distance indicators. SNe IIP are 1–2 mag less luminous than the SNe Ia; however, their intrinsic rate is higher than the SNe Ia rate (Li et al. 2011), and additionally the rate peaks at higher redshifts than SNe Ia (Taylor et al. 2014), which motivates their use in the cosmic distance scale (see Hamuy & Pinto 2002). Also, the fact that they are in principle the result of the same physical mechanism and, their progenitors are better understood than those of SNe Ia, further encourages investigations in this direction. SNe IIP are thought to be core-collapse supernovae (CCSNe), i.e., the final explosion of stars with zero-age main-sequence mass $\geqslant 8\,M_\odot$ (Smartt 2009). CCSNe have diverse classes, with a large range of observed luminosities, light curve shapes, and spectroscopic features. CCSNe are classified in two groups according to the absence (SNe Ib/c: Filippenko et al. 1993; Dessart et al. 2011; Bersten et al. 2014; Kuncarayakti et al. 2015) or presence (SNe II) of H I lines (Minkowski 1941; Filippenko 1997 and references therein). In addition to the SNe IIP and SNe IIL which are discussed later, SNe II are composed by SNe IIb that evolve spectroscopically from SNe IIP at early times to H I-deficient at a few weeks to a month past maximum (Woosley et al. 1987) and SNe IIn which have narrow H I emission lines (Chevalier 1981; Fransson 1982; Schlegel 1990; Chugai & Danziger 1994; Van Dyk et al. 2000; Kankare et al. 2012; de Jaeger et al. 2015).

Historically, SNe II were separated in two groups: SNe IIP (70% of CCSNe; Li et al. 2011), which are characterized by long duration plateau phases ($\leqslant 100$ days) of constant luminosity, and SNe IIL, which have linearly declining light curve morphologies (Barbon et al. 1979). However, as discussed in detail in Anderson et al. (2014b), it is not clear how well this terminology describes the diversity of SNe II. There are few SNe II that show flat light curves, and in addition there are very few (if any) SNe that decline linearly before falling onto the radioactive tail. Therefore, henceforth we simply refer to all SNe with distinct decline rates collectively as SNe II, and will later further discuss SNe in terms of their "s_2" plateau decline rates (Anderson et al. 2014b). Sanders et al. (2015) also suggested that the SNe II family forms a continuous class, while Arcavi et al. (2012) and Faran et al. (2014a, 2014b) have argued for two separate populations.

The most noticeable difference between SNe II occurs during the plateau phase. The optically thick phase is physically well understood and is due to a change in opacity and density in the outermost layers of the SN. At the beginning, the hydrogen present in the outermost layers of the progenitor star is ionized by the shock wave, which implies an increase of the opacity and the density, which prevent the radiation from the inner parts from escaping. After a few weeks, the star has cooled to temperatures allowing the recombination of ionized hydrogen (higher than 5000 K due to the large optical depth). The ejecta expand and the photosphere recedes in mass space, releasing the energy stored in the corresponding layers. The plateau morphology requires a recession of the photosphere in mass that corresponds to a fixed radius in space so that luminosity appears constant. As Anderson et al. (2014b) show, this delicate balance is rarely observed and there is significant diversity observed in the *V*-band light curve. To reproduce the plateau morphology, hydrodynamical models have used red supergiant progenitors with extensive H envelopes (Grassberg et al. 1971; Falk & Arnett 1977; Chevalier 1976). Direct detections of the progenitor of SNe IIP have confirmed these models (Van Dyk et al. 2003; Smartt et al. 2009). It has also been suggested that SN IIL progenitors may be more massive in the zero-age main sequence than SNe IIP (Elias-Rosa et al. 2010, 2011) and with smaller hydrogen envelopes (Popov 1993).

To date, several methods have been developed to standardize SNe II. The first method, called the expanding photosphere method (EPM), was developed by Kirshner & Kwan (1974) and allows one to obtain the intrinsic luminosity assuming that SNe II radiate as dilute blackbodies, and that the SN freely expands with spherical symmetry. The EPM was implemented for the first time on a large number of objects by Schmidt et al. (1994) and followed by many studies (Hamuy et al. 2001; Leonard et al. 2003; Dessart & Hillier 2005, 2006; Jones et al. 2009; Emilio Enriquez et al. 2011). One of the largest issues with this method is that the EPM only works if one corrects for the blackbody assumptions, which requires correction factors computed from model atmospheres (Eastman et al. 1996; Dessart & Hillier 2005; see Dessart & Hillier 2006 for the resolution of the EPM-based distance problem to SN 1999em). Also, to avoid the problem in the estimation of the dilution factor, Baron et al. (2004) proposed a distance-correcting factor that takes into account the departure of the SN atmosphere from a perfect blackbody, the spectral-fitting expanding atmosphere method" (SEAM; updated in Dessart et al. 2008). This method consists of fitting the observed spectrum using an accurate synthetic spectrum of SNe II, and then since the spectral energy distribution is completely known from the calculated synthetic spectra, one may calculate the absolute magnitude in any band.

A simpler method, also based on photometric and spectroscopic parameters, the standardised candle method (SCM), was first introduced by Hamuy & Pinto (2002). They found that the luminosity and the expansion velocity are correlated when the SN is in its plateau phase (50 days post-explosion). This relation is physically well understood: for a more luminous SN, the hydrogen recombination front will be at a larger radius, thereby the velocity of the photosphere will be greater (Kasen & Woosley 2009) for a given post-explosion time. Due to this method, the scatter in the Hubble diagram (hereafter Hubble diagram) drops from 0.8 to 0.29 mag in the *I* band. Nugent et al. (2006) improved this method by adding an extinction correction based on the $(V - I)$ color at day 50 after maximum. This new method is very powerful and many other studies (Nugent et al. 2006; Poznanski et al. 2009; D'Andrea et al. 2010; Olivares et al. 2010) have confirmed the possibility of using SNe II as standard candles finding a scatter between 10% and 18% in distance. Recently, Maguire et al. (2010)

suggested that using near-infrared (NIR) filters, the SCM, the dispersion can drop to a level of 0.1–0.15 mag (using 12 SNe IIP). Indeed, in the NIR the host galaxy extinction is less important, thus there may be less scatter in magnitude. Note also the work done by Rodríguez et al. (2014), where the authors used the photospheric magnitude method (PMM), which corresponds to a generalization of the SCM for various epochs throughout the photospheric phase, and found a dispersion of 0.12 mag using 13 SNe. This is an intrinsic dispersion and is not the root mean square (rms).

The main purpose of this work is to derive a method to obtain purely photometric distances, i.e., standardize SNe II only using light curves and color curve parameters, unlike other methods cited above which require spectroscopic parameters. This is a large issue, and purely photometric methods will be an asset for the next generation of surveys such as the large synoptic survey telescope (LSST; Ivezic et al. 2009; Lien et al. 2011). These surveys will discover such a large number of SNe that spectroscopic follow up will be impossible for all but only for small number of events. This will prevent the use of current methods to standardize SNe II and calculate distances. Therefore, deriving distances with photometric data alone is important and useful for the near future but also allows us to reach higher distance due to the fact that obtaining even one spectrum for a SN II at $z \geqslant 1$ is very challenging.

The paper is organized as follows. In Section 2 a description of the data set is given. In Section 3 we explain how the data are corrected for Milky Way (MW) extinction and how the K-correction (KC) is applied. In Section 4 we describe the photometric color method (PCM) using optical and NIR filters and we derive a photometric Hubble diagram. In Section 5 we present a comparative Hubble diagram using the SCM. In Section 6 we compare our method with the SCM and we conclude with a summary in Section 7.

2. DATA SAMPLE

2.1. Carnegie Supernova Project

The Carnegie Supernova Project[15] (CSP; Hamuy et al. 2006) provided all the photometric and spectroscopic data for this project. The goal of the CSP was to establish a high-cadence data set of optical and NIR light curves in a well defined and well understood photometric system and obtain optical spectra for these same SNe. Between 2004 and 2009, the CSP observed many low-redshift SNe II ($N_{SNe} \sim 100$ with $z \leqslant 0.04$), 56 of which had both optical and NIR light curves with good temporal coverage. This was one of the largest NIR data samples. Two SN 1987A-like events were removed (SN 2006V and SN 2006au; see Taddia et al. 2012), leaving the sample listed in Table 1 with photometric parameters measured by Anderson et al. (2014b). Note that we do not include SNe IIb or SNe IIn.

2.2. Data Reduction

2.2.1. Photometry

All the photometric observations were taken at the Las Campanas Observatory (LCO) with the Henrietta Swope 1 m and the Irénée du Pont 2.5 m telescopes using optical (u, g, r, i, B, and V) and NIR filters (Y, J, and H; see Stritzinger

et al. 2011). All optical images were reduced in a standard way including bias subtractions, flat-field corrections, application of a linearity correction, and an exposure time correction for a shutter time delay. The NIR images were reduced through the following steps: dark subtraction, flat-field division, sky subtraction, geometric alignment, and a combination of the dithered frames. Due to the fact that SN measurements can be affected by the underlying light of their host galaxies, we took care to correctly remove the underlying host galaxy light. The templates used for final subtractions were always taken months/years after each SN faded and under seeing conditions better than those of the science frames. Because the templates for some SNe were not taken with the same telescope, they were geometrically transformed to each individual science frame. These were then convolved to match the point-spread functions, and finally scaled in flux. The template images were then subtracted from a circular region around the SN position on each science frame (see Contreras et al. 2010).

Observed magnitudes for each SN were derived relative to local sequence stars and calibrated from observations of standard stars in the Landolt (1992; BV), Smith et al. (2002; u' $g'r'i'$), and Persson et al. (2004; $YJHKs$) systems. The photometry of the local sequence stars are on average based on at least three photometric nights. Magnitudes are expressed in the natural photometric system of the Swope+CSP bands. Final errors for each SN are the result of the instrumental magnitude uncertainty and the error on the zero point. The full photometric catalog will be published in an upcoming paper (note that the V-band photometry has already been published in Anderson et al. 2014b).

2.2.2. Spectroscopy

The majority of our spectra were obtained with the 2.5 m Irénée du Pont telescope using the WFCCD- and Boller and Chiven spectrographs (the last is now decommissioned) at LCO. Additional spectra were obtained with the 6.5 m *Magellan* Clay and Baade telescopes with LDSS-2, LDSS-3, MagE (see Massey et al. 2012 for details), and IMACS together with the CTIO 1.5 m telescope and the Ritchey-Chrétien Cassegrain Spectrograph, and the New Technology Telescope at La Silla observatory using the EMMI and EFOSC instruments. The majority of the spectra are the combination of three exposures to facilitate cosmic ray rejection. Information about the grism used, the exposure time, and the observation strategy can be found in Hamuy et al. (2006) and Folatelli et al. (2010). All spectra were reduced in a standard way as described in Hamuy et al. (2006) and Folatelli et al. (2013). Briefly, the reduction was done with IRAF[16] using the standard routines (bias subtraction, flat-field correction, one-dimensional (1D) extraction, and wavelength and flux calibration). The full spectroscopic sample will be published in an upcoming paper and the reader can refer to Anderson et al. (2014a) and Gutiérrez et al. (2014) for a thorough analysis of this sample.

3. FIRST PHOTOMETRIC CORRECTIONS

In order to proceed with our aim of creating a Hubble diagram based on photometric measurements using the PCM,

---

[16] IRAF is distributed by the National Optical Astronomy Observatory, which is operated by the Association of Universities for Research in Astronomy (AURA) under cooperative agreement with the National Science Foundation.

Table 1
SN II Parameters

SN	AvG (mag)	v_{helio} (km s^{-1})	v_{CMB} (km s^{-1})	Explosion Date (MJD)	s_1 (mag 100 day^{-1})	s_2 (mag 100 day^{-1})	OPTd (days)
2004ej	0.189	2723(6)	3045(23)	53224.90(5)	⋯	1.07(0.04)	96.14
2004er	0.070	4411(33)	4186(37)	53271.80(4)	1.28(0.03)	0.40(0.03)	120.15
2004fc	0.069	1831(5)	1560(20)	53293.50(10)	⋯	0.82(0.02)	106.06
2004fx	0.282	2673(3)	2679(3)	53303.50(4)	⋯	0.09(0.03)	68.40
2005J	0.075	4183(1)	4530(24)	53382.78(7)	2.11(0.07)	0.96(0.02)	94.03
2005Z	0.076	5766(10)	6088(25)	53396.74(8)	⋯	1.83(0.01)	78.84
2005an	0.262	3206(31)	3541(39)	53428.76(4)	3.34(0.06)	1.89(0.05)	77.71
2005dk	0.134	4708(25)	4618(26)	53599.52(6)	2.26(0.09)	1.18(0.07)	84.22
2005dn	0.140	2829(17)	2693(20)	53601.56(6)	⋯	1.53(0.02)	79.76
2005dw	0.062	5269(10)	4974(23)	53603.64(9)	⋯	1.27(0.04)	92.59
2005dx	0.066	8012(31)	7924(31)	53615.89(7)	⋯	1.30(0.05)	85.59
2005dz	0.223	5696(8)	5327(27)	53619.50(4)	1.31(0.08)	0.43(0.04)	81.86
2005es	0.228	11287(49)	10917(55)	53638.70(10)	⋯	1.31(0.05)	⋯
2005gk	0.154	8773(10)	8588(30)	⋯	⋯	1.25(0.07)	⋯
2005hd	0.173	8323(10)	8246(30)	⋯	⋯	1.83(0.13)	⋯
2005lw	0.135	7710(29)	8079(39)	53716.80(10)	⋯	2.05(0.04)	107.23
2006Y	0.354	10074(10)	10220(30)	53766.50(4)	8.15(0.76)	1.99(0.12)	47.49
2006ai	0.347	4571(10)	4637(30)	53781.80(5)	4.97(0.17)	2.07(0.04)	63.26
2006bc	0.562	1363(10)	1476(13)	53815.50(4)	1.47(0.18)	−0.58(0.04)	⋯
2006be	0.080	2145(9)	2243(11)	53805.81(6)	1.26(0.08)	0.67(0.02)	72.89
2006bl	0.144	9708(49)	9837(50)	53823.81(6)	⋯	2.61(0.02)	⋯
2006ee	0.167	4620(19)	4343(27)	53961.88(4)	⋯	0.27(0.02)	85.17
2006it	0.273	4650(9)	4353(23)	54006.52(3)	⋯	1.19(0.13)	⋯
2006ms	0.095	4543(18)	4401(21)	54034.00(13)	2.07(0.30)	0.11(0.48)	⋯
2006qr	0.126	4350(5)	4642(21)	54062.80(7)	⋯	1.46(0.02)	96.85
2007P	0.111	12224(25)	12570(35)	54118.71(3)	⋯	2.36(0.04)	84.33
2007U	0.145	7791(9)	7795(9)	54134.61(6)	2.94(0.02)	1.18(0.01)	⋯
2007W	0.141	2902(2)	3215(22)	54136.80(7)	⋯	0.12(0.04)	77.29
2007X	0.186	2837(6)	3055(16)	54143.85(5)	2.43(0.06)	1.37(0.03)	97.71
2007aa	0.072	1465(4)	1826(26)	54135.79(5)	⋯	−0.05(0.02)	67.26
2007ab	0.730	7056(13)	7091(13)	54123.86(6)	⋯	3.30(0.08)	71.30
2007av	0.099	1394(3)	1742(24)	54175.76(5)	⋯	0.97(0.02)	⋯
2007hm	0.172	7540(15)	7241(26)	54335.64(6)	⋯	1.45(0.04)	⋯
2007il	0.129	6454(10)	6146(24)	54349.77(4)	⋯	0.31(0.02)	103.43
2007oc	0.061	1450(5)	1184(19)	54382.51(3)	⋯	1.83(0.01)	77.61
2007od	0.100	1734(3)	1377(25)	54402.59(5)	2.37(0.05)	1.55(0.01)	⋯
2007sq	0.567	4579(4)	4874(21)	54421.82(3)	⋯	1.51(0.05)	88.34
2008F	0.135	5506(21)	5305(25)	54470.58(6)	⋯	0.45(0.10)	⋯
2008K	0.107	7997(10)	8351(27)	54477.71(4)	⋯	2.72(0.02)	87.1
2008M	0.124	2267(4)	2361(8)	54471.71(9)	⋯	1.14(0.02)	75.34
2008W	0.267	5757(45)	6041(49)	54485.78(6)	⋯	1.11(0.04)	83.86
2008ag	0.229	4439(6)	4428(6)	54479.85(6)	⋯	0.16(0.01)	102.95
2008aw	0.111	3110(4)	3438(23)	54517.79(10)	3.27(0.06)	2.25(0.03)	75.83
2008bh	0.060	4345(8)	4639(22)	54543.54(5)	3.00(0.27)	1.20(0.04)	⋯
2008bk	0.054	230(4)	−50(20)	54542.89(6)	⋯	0.11(0.02)	104.83
2008bu	1.149	6630(9)	6683(10)	54566.78(5)	⋯	2.77(0.14)	44.75
2008ga	1.865	4639(3)	4584(5)	54711.85(4)	⋯	1.17(0.08)	72.79
2008gi	0.181	7328(34)	7103(37)	54742.72(9)	⋯	3.13(0.08)	⋯
2008gr	0.039	6831(41)	6549(46)	54766.55(4)	⋯	2.01(0.01)	⋯
2008hg	0.050	5684(10)	5449(19)	54779.75(5)	⋯	−0.44(0.01)	⋯
2009N	0.057	1036(2)	1386(25)	54846.79(5)	⋯	0.34(0.01)	89.50
2009ao	0.106	3339(5)	3665(23)	54890.67(4)	⋯	−0.01(0.12)	41.71
2009bu	0.070	3494(9)	3372(13)	54907.91(6)	0.98(0.16)	0.18(0.04)	⋯
2009bz	0.110	3231(7)	3393(13)	54915.83(4)	⋯	0.50(0.02)	⋯

Note. SN and light curve parameters. In column 1, the SN name, followed by its reddening due to dust in our Galaxy (Schlafly & Finkbeiner 2011), are listed. In column 3, we list the host galaxy heliocentric recession velocity. These are taken from the NASA Extragalactic Database (NED: http://ned.ipac.caltech.edu/). In column 4, we list the host galaxy velocity in the CMB frame using the CMB dipole model presented by Fixsen et al. (1996). In column 5, the explosion epochs is presented. In columns 6 and 7, we list the decline rate s_1 and s_2 in the V band, where s_1 is the initial steeper slope of the light curve and s_2 is the decline rate of the plateau as defined by Anderson et al. (2014b). Finally, column 8 presents the optically thick phase duration (OPTd) values, i.e., the duration of the optically thick phase from explosion to the end of the plateau (see Anderson et al. 2014b).

in this section we show how to correct apparent magnitudes for MW extinction (AvG) and how to apply the KC without the use of observed SN spectra but only with model spectra.

3.1. MW Correction

In the V band the determination of AvG can be applied using the extinction maps of Schlafly & Finkbeiner (2011). To convert AvG to extinction values in other bands, we need to adopt an extinction law and the effective wavelength for each filter.

SN II spectra evolve with time from a blue continuum at early times to a redder continuum with many absorption/ emission features at later epochs. This implies that the effective wavelength of a broadband filter also changes with time (see the formula given Bessell & Murphy 2012, A.21). To calculate effective wavelengths at different epochs, we adopt a sequence of theoretical spectral models from Dessart et al. (2013) consisting of a SN progenitor with a main-sequence mass of $15\,M_\odot$, solar metallicity $Z = 0.02$, zero rotation, and a mixing length parameter of 3.[17] The choice of this model is based on the fact that it provided a good match to a prototypical SN II such as SN 1999em. For each photometric epoch, we choose the closest theoretical spectrum in each epoch since the explosion, the extinction law from Cardelli et al. (1989), and in time $R_V = 3.1$ to obtain the MW extinction in the other filters.

3.2. K-correction

Having corrected the observed magnitudes for Galactic extinction, we also need to apply a correction attributable to the expansion of the universe called the KC. A photon received in one broad photometric bandpass in the observed referential has not necessarily been emitted (rest-frame referential) in the same filter, which is why this correction is needed. For each epoch of each filter we use the same procedure to estimate the KC. Here we describe our method step by step for one epoch and a given filter X.

1. We choose in our model spectral library (Dessart et al. 2013, model m15mlt3) the theoretical spectrum (rest frame) closest to the photometric epoch since the explosion time (corrected for time dilatation), with a rest-frame spectral energy distribution (SED), $f^{\rm rest}(\lambda_{\rm rest})$. Because our library covers a limited range of epochs from 12.2 to 133 days relative to explosion, observations outside these limits are ignored.

2. We bring the rest-frame theoretical spectrum to the observer's frame using the $(1 + z_{\rm hel})$ correction, where $z_{\rm hel}$ is the heliocentric redshift of the SN, $f^{\rm obs}(\lambda) = f^{\rm rest}(\lambda_{\rm rest}(1 + z_{\rm hel})) \times 1/(1 + z_{\rm hel})$, where λ is the wavelength in the observer's frame.

3. We match the theoretical spectrum to the observed photometric magnitudes of the SN (Hsiao et al. 2007). For this we calculate synthetic magnitudes (from the model in the observer's frame, $f^{\rm obs}(\lambda)$) and compare them to the observed magnitudes corrected for MW extinction. We use all the filters available at this epoch. Then we obtain a warping function $W(\lambda)$ (quadratic, cubic, depending on the number of filters used) and do a constant extrapolation for the wavelengths outside of the
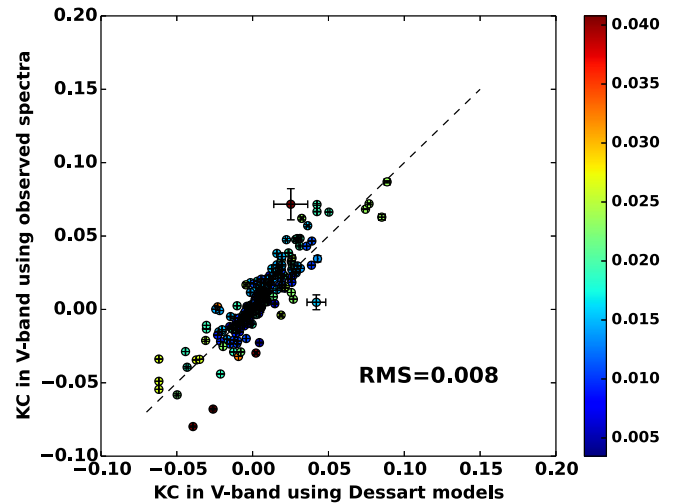

Figure 1. Comparison between the KC calculated using the theoretical models and observed spectra at different redshifts in the V band. The black dotted line represents $x = y$. Each square represents one observed spectrum of our database. The color bar on the right side represents the different redshifts.

range of filters used. With our warping function, we correct our model spectrum and obtain $f^{\rm obs}_{\rm warp}(\lambda) = W(\lambda) \times f^{\rm obs}(\lambda)$. We compute the magnitude in the observer's frame:

$$m_z^X = -2.5 \log_{10}\left(\frac{1}{hc} \int f^{\rm obs}_{\rm warp}(\lambda) S_\lambda^X \lambda d\lambda \right) + {\rm ZP}_X,$$

where c is the light velocity in Å s^{-1}, h the Planck constant in erg s, λ is wavelength, S_λ^X the transmission function of filter X, and ${\rm ZP}_X$ is the zero point of filter X (see Contreras et al. 2010; Stritzinger et al. 2011).

4. We bring back the warping spectrum to the rest frame $f^{\rm rest}_{\rm warp}(\lambda) = (1 + z_{\rm hel}) f^{\rm obs}_{\rm warp}(\lambda \times 1/(1 + z_{\rm hel}))$ and we obtain and calculate the magnitude:

$$m_0^X = -2.5 \log_{10}\left(\frac{1}{hc} \int f^{\rm rest}_{\rm warp}(\lambda) S_\lambda^X \lambda d\lambda \right) + {\rm ZP}_X.$$

5. Finally, we obtain the KC for this epoch as the difference between the observed and the rest-frame magnitude, ${\rm KC}_X = m_z^X - m_0^X$.

6. To estimate the associated errors, we follow the same procedure but instead of using the observed magnitudes for the warping, we use the upper limit, i.e., observed magnitudes plus associated uncertainties.

As a complementary work on the KC and to validate our method, we compare the KC values found using the Dessart et al. (2013) model to those computed from our database of observed spectra. In both cases we use exactly the same procedure. First, the observed spectrum is corrected in flux using the observed photometry (corrected for AvG) in order to match the observed magnitudes. The photometry is interpolated to the spectral epoch. In Figure 1 we show a comparison between the KC obtained with the theoretical models and using our library of observed spectra at different redshifts. As we can see, the KC values calculated with both methods are very consistent. This exercise validates the choice of using the Dessart et al. (2013) models to calculate the KC. There are two advantages to use the theoretical models. First, we can obtain the KC for NIR filters (Y, J, H) for which we do not have

---

[17] More information about this model (named m15mlt3) can be found in Dessart et al. (2013).

observed spectra, and second, this method does not require observed spectra which are expensive to obtain in terms of telescope time, and virtually impossible to get at higher redshifts.

4. THE PHOTOMETRIC COLOR METHOD: PCM

In this section, we present our PCM with which we derive the corrected magnitudes necessary for constructing the Hubble diagram solely with photometric data. Since we want to examine Hubble diagrams from photometry obtained at different epochs, we start by linearly interpolating colors on a daily basis from colors observed at epochs around the epoch of interest. The same procedure is used to interpolate magnitudes.

4.1. Methodology

To correct and standardize the apparent magnitude, we use two photometric parameters: s_2, which is the slope of the plateau measured in the V band (Anderson et al. 2014b), and a color term at a specific epoch. The color term is mainly used to take into account the dispersion caused by the host galaxy extinction. The magnitude is standardized using a weighted least-squares routine by minimizing the equation below:

$$m_{\lambda 1} + \alpha s_2 - \beta_{\lambda 1}(m_{\lambda 2} - m_{\lambda 3}) = 5 \log(cz) + \text{ZP}, \qquad (1)$$

where c is the speed of light, z the redshift, $m_{\lambda_{1,2,3}}$ the observed magnitudes with different filters, and corrected for AvG and KC, while α, β_{λ_1}, and ZP are free-fitting parameters. The errors on these parameters are derived assuming a reduced chi square equal to one. In order to obtain the errors on the standardized magnitudes, an error propagation is performed in an iterative manner. Note that β_{λ_1} is related to host galaxy R_V if we assume that the color–magnitude relation is due to extrinsic factors (the intrinsic color is degenerate with the ZP). We obtain:

$$\beta_{\lambda 1} = \frac{A_{\lambda 1}}{E(m_{\lambda 2} - m_{\lambda 3})}, \qquad (2)$$

where $A_{\lambda 1}$ is the host galaxy extinction in the $\lambda 1$ filter and E the color excess. Assuming a Cardelli et al. (1989) law, there is a one-to-one relationship between R_V and β_{λ_1}. First we obtain the theoretical β for different R_V values using the Cardelli et al. (1989) coefficients (a and b):

$$\beta(R_V) = \frac{a_{\lambda 1} + \dfrac{b_{\lambda 1}}{R_V}}{\left(a_{\lambda 2} + \dfrac{b_{\lambda 2}}{R_V}\right) - \left(a_{\lambda 3} + \dfrac{b_{\lambda 3}}{R_V}\right)}. \qquad (3)$$

Then we derive R_V from the value of $\beta_{\lambda 1}$ determined from the least-squares fit (Equation (1)). We will discuss the resulting R_V values in Section 6.5.

4.2. Hubble Flow Sample

We select only SNe located in the Hubble flow, i.e., with $cz_{\text{CMB}} \geqslant 3000 \,\text{km s}^{-1}$ in order to minimize the effect of peculiar galaxy motions. Our available sample is composed of the entire sample in the Hubble flow except for 3 SNe. We eliminate two SNe due to the fact that the warping function cannot be computed, thus the KC (SN 2004ej and SN 2008K). We also take out the outlier SN 2007X and found for this object particular characteristics like clear signs of interaction
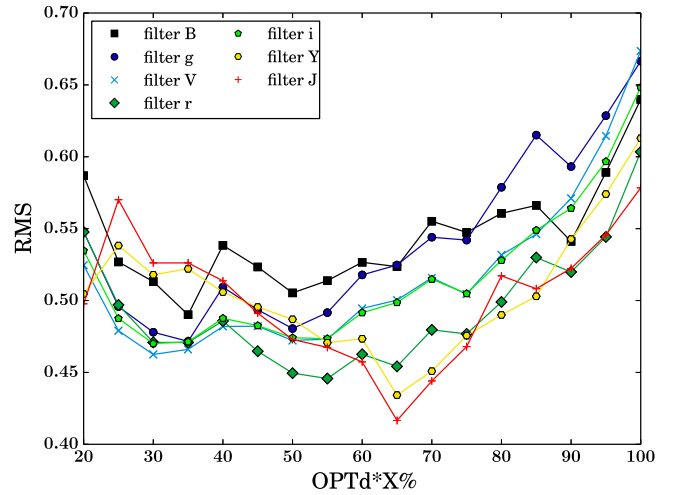

Figure 2. Variation in phase of the dispersion in the Hubble diagram for different filters and using a color term $(V - i)$. In the x axis we present the time as (explosion time+OPTd*X%). The black squares represent the B band, dark blue circles the g band, blue crosses the V band, dark green diamonds the r band, green hexagons the i band, yellow pentagons the Y band, and red plus signs the J band. The H band is not represented because the sampling is as good as it is in the other bands.

with the circumstellar medium (flat H alpha P-Cygni profile; see C. P. Gutiérrez et al. 2016, in preparation).

SNe II are supposedly characterized by similar physical conditions (e.g., temperature) when they arrive toward the end of the plateau (Hamuy & Pinto 2002), which is why we use the end of the optically thick phase measured in the V band (as defined by Anderson et al. 2014b) as the time origin in order to bring all SNe to the same timescale. When the end of the plateau is not available, we choose 80 days post-explosion, which is the average for our sample.

Given that SNe II show a significant dispersion in the plateau duration driven by different evolution speeds, we decide to take a fraction of the plateau duration and not an absolute time to ensure that we compare SNe II at the same evolutionary phase. Thus, in the following analysis, we adopt OPTd*X% as the time variable where OPTd is the optically thick phase duration and X is percentage ranging between 1% and 100%.

In Figure 2 we present the variation with evolutionary phase of the dispersion in the Hubble diagram using the filters available and the $(V - i)$ color. The lowest rms values in the optical is found for the r band, and at NIR wavelength using the Y/J band. Note that the coverage in the Y band is better than in the J band, hence hereafter we use the Y band. For these two bands we can obtain the median rms over all the epochs (from 0.2*OPTd to 1.0*OPTd) and the standard deviation. We find for the r band $0.47 \pm 0.04 \,\text{mag}$ and for the Y band $0.48 \pm 0.04 \,\text{mag}$. In Figure 3 we do the same as above but we change colors. Fixing the r band and using different colors, we show the variation of the rms. This figure shows that the color that minimizes the rms is $(V - i)$ $((r - J)$ yields a lower dispersion but the time coverage is significantly less). We find a median rms over all the epochs of 0.47 ± 0.05. For this reason we decide to combine the r band and the $(V - i)$ color for the Hubble diagram. Note also that the best epoch for the r band is close to the middle of the plateau, 55% of the time from the explosion to the end of the plateau, whereas the best epoch in the Y band is later in phase post-explosion, around 65%. In
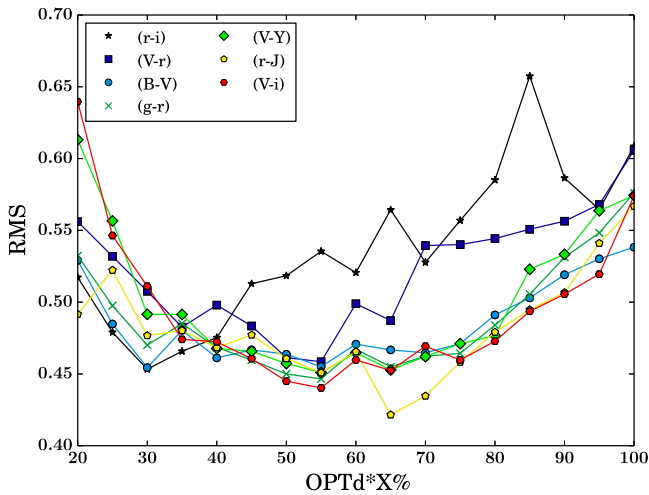
Figure 3. Variation in phase of the dispersion in the Hubble diagram using the r band and different colors. In the x axis we present the time as the OPTd$^+$X%. The black stars represent $(r-i)$ color, dark blue squares $(V-r)$, blue circles $(B-V)$, cyan crosses $(g-r)$, green diamonds $(V-Y)$, yellow pentagons $(r-J)$, and red hexagons $(V-i)$.

general, the best epoch to standardize the magnitude is between 60% and 70% of the OPTd for NIR filters and for optical filters between 50% and 60% of OPTd. Physically these epochs correspond in both cases more or less to the middle of the plateau. Note that we tried other time origins such as the epoch of maximum magnitude instead of the end of the plateau, but changing the reference does not lower the rms.

In Figure 4 we present a Hubble diagram based entirely on photometric data using s_2 and color term for two filters, the r band and the Y band. In the r band the rms is 0.44 mag (with 38 SNe) which allows us to measure distances with an accuracy of ~20%. We find the same precision using the Y' band with a rms of 0.43 mag (30 SNe). Note that the color term is more important for the optical filter than for the NIR filter. Indeed, for the r band the rms decreases from 0.50 to 0.44 mag when the color term is added, whereas for the NIR filter the improvement is only of 0.004 mag. Using all available epochs, we find a mean improvement of 0.025 ± 0.011 in the r band and 0.014 ± 0.013 in the Y band. This shows that the improvement is significant in the optical but less in the NIR. The drop using the optical filter is not surprising because this term is probably at least partly related to host galaxy extinction which is more prevalent in optical wavelengths than in the NIR, so adding a color term for NIR filters does not significantly influence the dispersion. Note that if we use the weighted root mean square (WRMS) as defined by Blondin et al. (2011) we find 0.40 mag and 0.36 mag for the r band and Y band, respectively, after s_2 and color corrections.

In the literature, a majority of the studies used SNe IIP for their sample. To check if we can include all the SNe II (fast and slow decliners), we did some analysis of the SNe and investigate if any of the higher residuals arise from intrinsic SN properties. The overall conclusion is that, at least to first order, we did not find any correlation between SNe II intrinsic differences (s_2, OPTd,...) and the Hubble residuals. This suggests that SNe within the full range of s_2 values (i.e., all SNe II) should be included in Hubble diagram.

Following the work of Folatelli et al. (2010) for SNe Ia, we investigated the combined Hubble diagram using all the filters available (by averaging the distance moduli derived in each

filter) but the dispersion obtained is not much better. We found the same correlation between the distance modulus residuals in one band versus those in another band, as found by Folatelli et al. (2010), suggesting that the inclusion of multiple bands does not improve the distance estimate.

If we include SNe in the Hubble flow ($cz \geqslant 3000\,\mathrm{km\,s^{-1}}$) and very nearby SNe ($cz \leqslant 3000\,\mathrm{km\,s^{-1}}$) for the r band, the dispersion increases from 0.44 to 0.48 mag (46 SNe), whereas in the Y band the rms increase from 0.43 mag to 0.45 (41 SNe).

We also try to use two different epochs, one for the magnitude and the other for the color, but again this does not improve the rms. Finally, we try also to use the total decline rate (between maximum to the end of the plateau) instead of the plateau slope. Using the total decline rate does not lower the rms (dispersion around 0.47 mag for 45 SNe in the r band) but could be useful for high redshift SNe.

5. THE STANDARD CANDLE METHOD (SCM)

The SCM as employed by various authors gives a Hubble diagram dispersion of 0.25–0.30 mag (Hamuy & Pinto 2002; Nugent et al. 2006; Poznanski et al. 2009; D'Andrea et al. 2010; Olivares et al. 2010). Here we present the Hubble diagram using the SCM for our sample.

5.1. Fe II Velocity Measurements

To apply the SCM, we need to measure the velocity of the SN ejecta. One of the best features is Fe II λ 5018 because other iron lines such as Fe II λ 5169 can be blended by other elements. Expansion velocities are measured through the minimum flux of the absorption component of P-Cygni line profile after correcting the spectra for the heliocentric redshifts of the host galaxies. Errors were obtained by measuring many times the minimum of the absorption changing the trace of the continuum. The range of velocities is 1800–8000 km s^{-1} for all the SNe. Because we need the velocities for different epochs in order to find the best epoch (as done for the PCM), i.e., with less dispersion, we do an interpolation/extrapolation using a power law (Hamuy 2001) of the form:

$$V(t) = A \times t^{\gamma}, \qquad (4)$$

where A and γ are two free parameters obtained by least-squares minimization for each individual SN and t the epoch since explosion. In order to obtain the velocity error, we perform a Monte Carlo simulation, varying randomly each velocity measurement according to the observed velocity uncertainties over more than 2000 simulations. From this, for each epoch (from 1 to 120 days after explosion) we choose the velocity as the average value and the incertainty to the standard deviation of the simulations. The median value of γ is -0.55 ± 0.25. This value is comparable with the value found by other authors (-0.5 for Olivares et al. 2010, -0.464 by Nugent et al. 2006, and -0.546 by Takáts & Vinkó 2012). Note that, as found by Faran et al. (2014a), the iron velocity for the fast decliners (SNe IIL) also follow a power law but with more scatter. Indeed, for the slow decliners ($s_2 \leqslant 1.5$), we find a median value $\gamma = -0.55 \pm 0.18$, whereas for the fast decliners ($s_2 \geqslant 1.5$) we obtain $\gamma = -0.56 \pm 0.35$. More details will be published in an upcoming paper (Gutiérrez et al.).
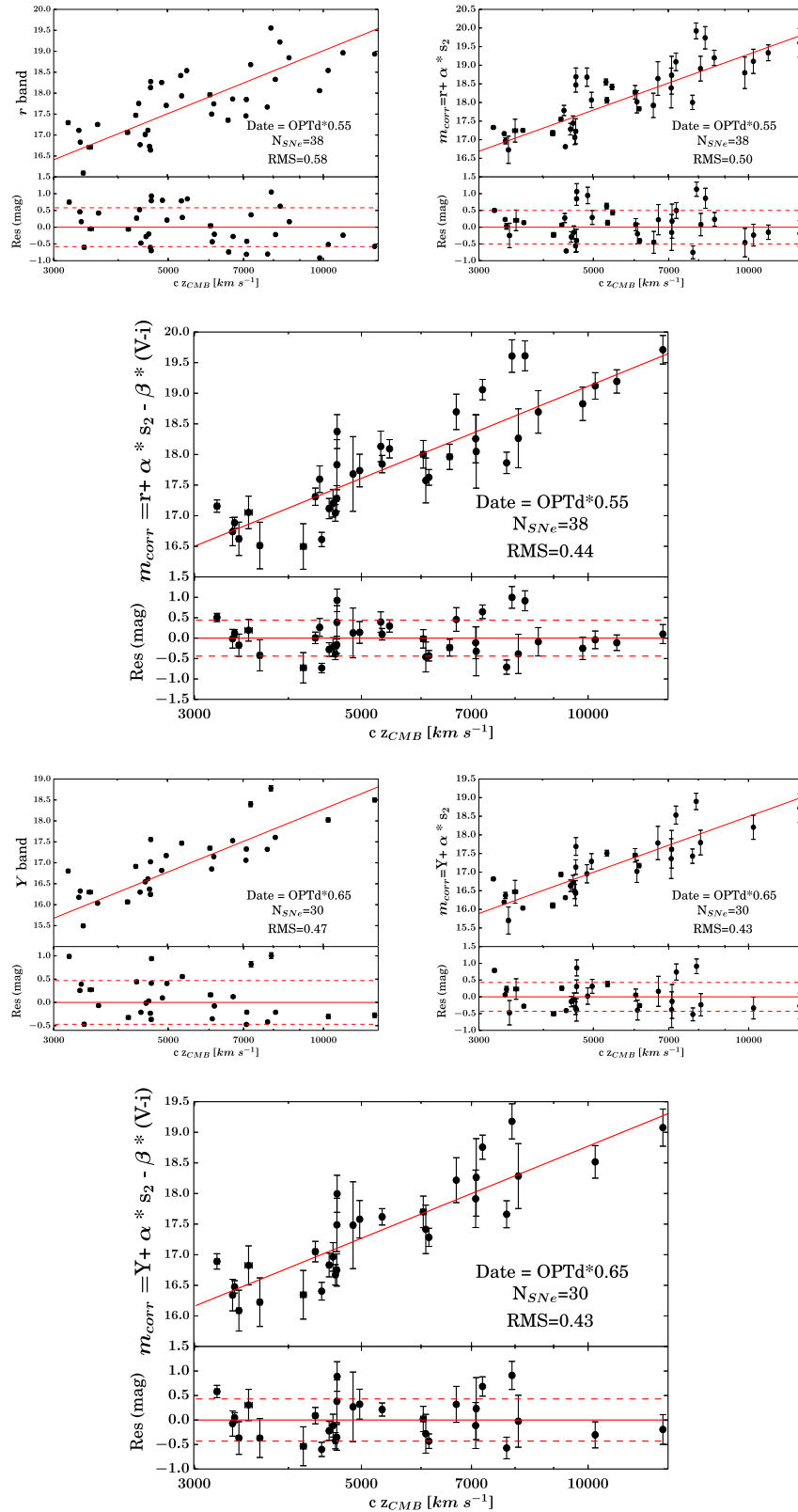
Figure 4. In the figures, we present the dispersion (rms) using the PCM, the number of SNe (N_{SNe}), and the epoch chosen with respect to OPTd (OPTd*X%) for our Hubble flow sample. On the bottom of each plot, the residuals are shown. In all the residual plots, the dashed line correspond to the rms. Top left: apparent magnitude corrected for MW extinction and KC in the r band plotted against cz_{CMB}; Top right: apparent magnitude corrected for MW extinction, KC and s_2 term in the r band plotted against cz_{CMB}. Top center: apparent magnitude corrected for MW extinction, KC, s_2 term in the r band, and by color term, $(V - i)$ plotted against cz_{CMB}. Bottom left: apparent magnitude corrected for MW extinction and KC in the Y band plotted against cz_{CMB}; Bottom right: apparent magnitude corrected for MW extinction, KC and s_2 term in the Y band plotted against cz_{CMB}. Bottom center: apparent magnitude corrected for MW extinction, KC, s_2 term in the Y band, and by color term $(V - i)$ plotted against cz_{CMB}.

5.2. Methodology

To standardize the apparent magnitude, we perform a least-squares minimization on:

$$m_{\lambda 1} + \alpha \log\left(\frac{v_{\text{Fe II}}}{5000 \text{ km s}^{-1}}\right) - \beta_{\lambda_1}(m_{\lambda 2} - m_{\lambda 3})$$
$$= 5 \log(cz) + \text{ZP}, \quad (5)$$

where c, z, and $m_{\lambda 1,2,3}$ are defined in Section 4.1 and α, β_{λ_1}, and ZP are free-fitting parameters. The errors on the magnitude are obtained in the same way as for the PCM but the epoch is different. For the SCM, the photospheric expansion velocity is very dependent on the explosion date. This is why, after trying different epochs and references, we found that the best reference is the explosion time as used in Nugent et al. (2006), Poznanski et al. (2009), and Rodríguez et al. (2014). The same epoch for the magnitude, color, and iron velocity is employed. Just like for the PCM, we use the same color, $(V - i)$ and the same filters (r, Y band). For some SNe, we are not able to measure an iron velocity due to the lack of spectra (only one epoch) and our sample is thus composed of 26 SNe.

5.3. Results

In Figure 5 we present the Hubble diagram and the residual for two different filters. The dispersion is 0.29 mag (or 0.30–0.28 mag in WRMS for the Y band and r band, respectively) for 24 SNe (some SNe do not have color at this epoch). These values are somewhat better than previous studies (Hamuy & Pinto 2002; Nugent et al. 2006; Poznanski et al. 2009; D'Andrea et al. 2010; Olivares et al. 2010) where the authors found dispersions around 0.30 mag with 30 SNe (more details in Section 6.3). Note the major differences between our study and theirs is that they included very nearby SNe ($cz \leqslant 3000$ km s^{-1}), only slow declining SNe II (SNe II with low s_2, historically referred to as SNe IIP), did not calculate a power law for each SN as we do, and used a different epoch. Note also the work done by Maguire et al. (2010), where they applied the SCM to NIR filters (J band and $(V - J)$ color) using nearby SNe (92% of their sample with $cz \leqslant 3000$ km s^{-1}), finding a dispersion of 0.39 mag with 12 SNe (see Section 6.3). To finish, we tried a combination of the PCM and SCM, i.e., adding a s_2 term to the SCM but this does not improve the dispersion.

6. DISCUSSION

Above we demonstrate that using two terms, s_2 and color, we are able to obtain a dispersion of 0.43 mag (optical bands). In this section, we try to reduce the rms by using well observed SNe and we compare the PCM to the SCM. We also discuss comparisons between the SCM using the CSP sample with other studies. Because the value of the rms is the crucial parameter to estimate the robustness of the method, we also discuss statistical errors. Finally, we briefly present the values of R_V derived from the color term both from PCM and SCM.

6.1. Golden Sample

A significant fraction of values from Anderson et al. (2014b) do not correspond to the slope of the plateau but sometimes to a combination of s_1 (initial decline) and s_2. Indeed, for some SNe, it was impossible to distinguish two slopes and the best fit
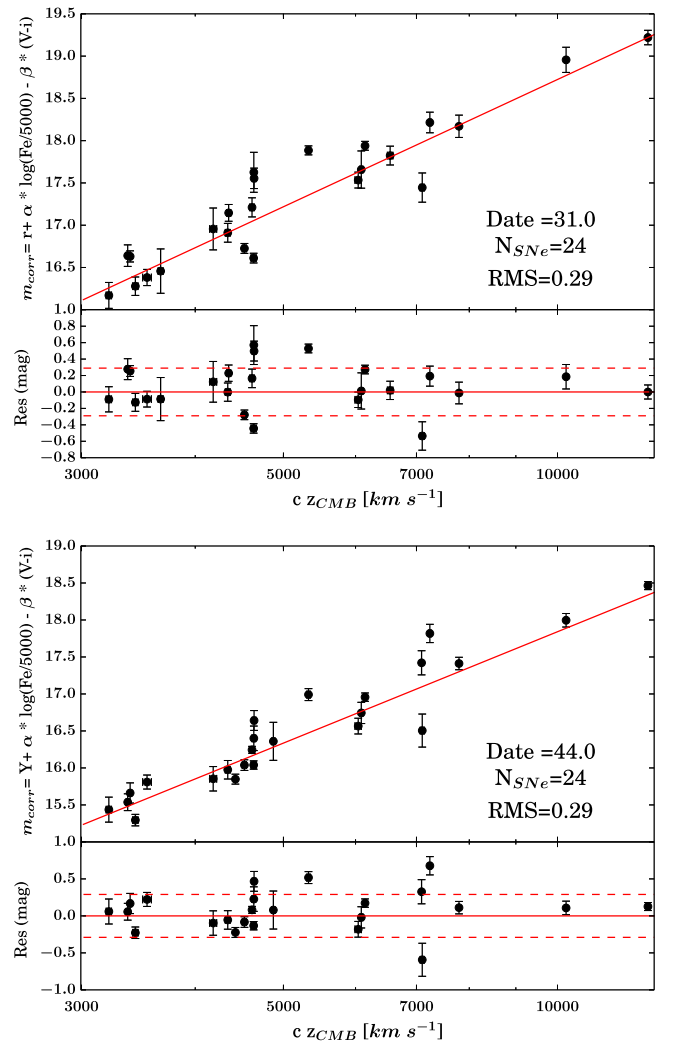

Figure 5. In all the figures, we present the dispersion (rms) using the SCM. The number of SNe (N_{SNe}) and the epoch chosen with respect to the explosion date in days. Both plots present the Hubble diagram using the SNe in the Hubble flow. On the top we present the Hubble diagram using the r band and the color $(V - i)$. On the bottom is the same but we use a NIR filter, Y band. On the bottom of each plot we present the residual. In the residuals plot, the dashed line correspond to the rms.

was only one slope. For this reason, we decide to define a new sample composed only by 12 SNe with values of s_1 and s_2 and with $cz_{\text{CMB}} \geqslant 3000$ km s^{-1}. From this sample and using the $r/(V - i)$ combination, we obtain a dispersion of 0.39 mag with 12 SNe, which compares to 0.48 mag from the entire sample. From the Y band, the dispersion drops considerably from 0.44 to 0.18 mag with only 8 SNe. However, this low value should be taken with caution due to possible statistical effects which are discussed later (see Section 6.4).

6.2. Method Comparisons

In Figures 6 and 7 we compare the Hubble diagram obtained using the SCM and the PCM. For both methods we use the same SNe (Hubble flow sample) and the same set of magnitude–color. The dispersion using the r band and the Y band is 0.43 mag for the PCM, whereas for the SCM is 0.29.

In general, the SCM is more precise than the PCM but the dispersion found with the PCM is consistent with the results found by the theoretical studies done by Kasen & Woosley
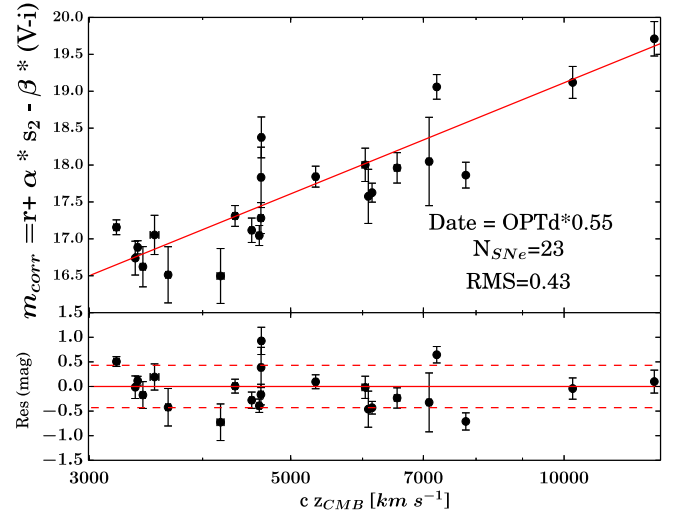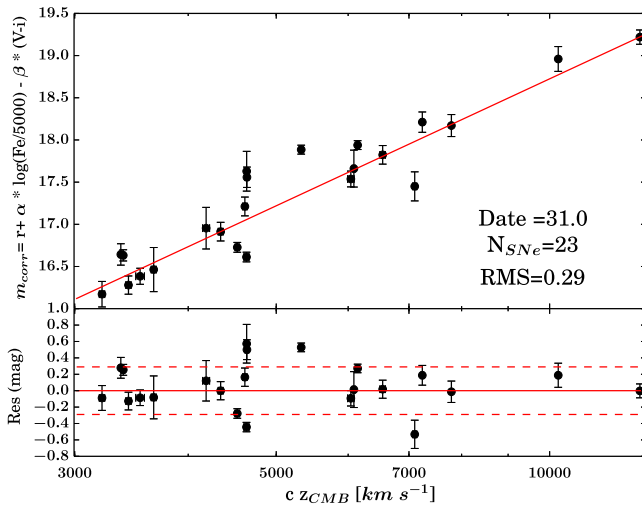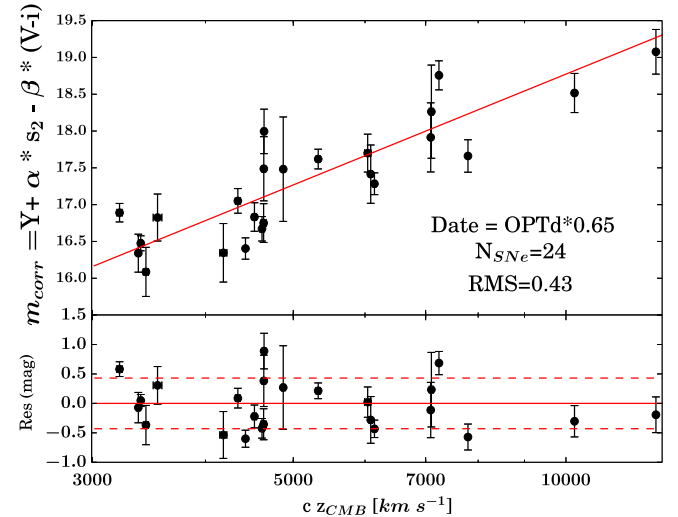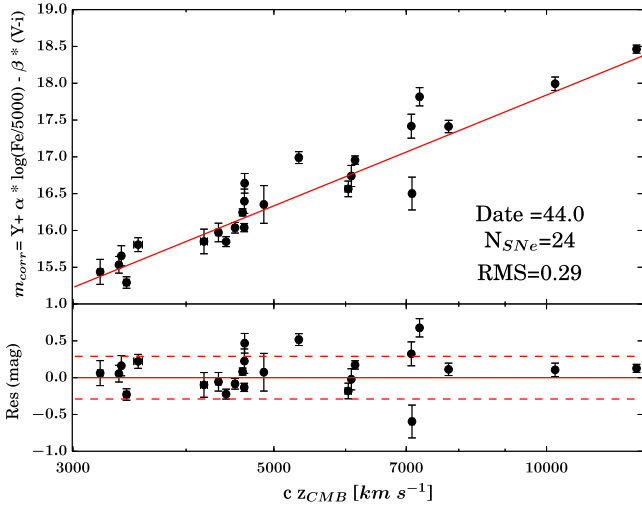
Figure 6. In all the figures, we present the dispersion (rms), the number of SNe (N_{SNe}), and the epoch chosen with respect to the end of the plateau (OPTd*X%) for the SCM and with respect to the explosion date for the SCM. On the bottom of each plot, the residuals are shown. In all the residual plots, the dashed line correspond to the rms. For both methods we use the Hubble flow sample, $cz_{CMB} \geqslant 3000$ km s^{-1}, the r band and the color ($V - i$). Plotted on the left is the SCM whereas in the right is for the PCM.

Figure 7. In all the figures, we present the dispersion (rms), the number of SNe (N_{SNe}), and the epoch chosen with respect to the end of the plateau (OPTd*X%) for the SCM and with respect to the explosion date for the SCM. On the bottom of each plot, the residuals are shown. In all the residual plots, the dashed line correspond to the rms. For both methods we use the Hubble flow sample, $cz_{CMB} \geqslant 3000$ km s^{-1}, the Y band and the color ($V - i$). Plotted on the left is the SCM whereas in the right is for the PCM.

(2009; distances accurate to ~20%) but the authors used other photometric correlations (plateau duration). Unfortunately, as suggested by Anderson et al. (2014b), using this parameter the prediction is not seen in the observations. We tried to use the OPTd values as an input instead of the s_2 and we did not see any improvement on the dispersion. Note also the recent work of Faran et al. (2014b), in which the authors found a correlation between the iron velocity and the I-band total decline rate. Although in this paper we do not use the total decline rate but another quantity related to the plateau slope, our work confirms the possibility of using photometric parameters instead of spectroscopic.

6.3. SCM Comparisons

In this section we compare our SCM with other studies. First, we use only optical filters to compare with Poznanski et al. (2009) and Olivares et al. (2010). Both studies used

the ($V - I$) color and also the I band. Note that Olivares et al. (2010) also used the B and V bands but here we consider only the I band for consistency. Poznanski et al. (2009) found a dispersion of 0.38 mag using 40 slow decliners. In our sample, instead of using the I band we used the sloan filter, i band, and ($V - i$) color. Using our entire sample, i.e., SNe (37 SNe in total for all the redshift range), we derive a dispersion similar to Poznanski et al. (2009) of 0.32 mag (epoch: 35 days after explosion). We can also compare the parameter α derived from the fit. Again we obtain a consistent value, $\alpha = 4.40 \pm 0.52$, whereas Poznanski et al. (2009) found $\alpha = 4.6 \pm 0.70$. The other parameters are not directly comparable due to the fact that the authors assumed an intrinsic color which is not the case in the current work. Using a Hubble constant (H_0) equal to 70 km s^{-1} Mpc^{-1}, we can translate our ZP to an absolute magnitude (ZP = $M_{corr} - 5\log(H_0) + 25$) $M_i = -17.12 \pm 0.10$ mag that it is lower than the results

obtained by Poznanski et al. (2009; $M_I = -17.43 \pm 0.10$ mag). This difference is probably due to the fact that the corrected magnitude has not been corrected for the intrinsic color in our work.

Using 30 slow declining SNe in the Hubble flow and very nearby SNe (z between 0.00016 and 0.05140), $(V - I)$ color, and the I band, Olivares et al. (2010) derived a dispersion of 0.32 mag which is the same as what we obtained. However, the parameters derived by Olivares et al. (2010) are different. Indeed, using the same Equation (5) and the entire sample they obtained $\alpha = 2.62 \pm 0.21$, $\beta = 0.60 \pm 0.09$, and ZP $= -2.23 \pm 0.07$ instead of $\alpha = 4.40 \pm 0.52$, $\beta = 0.98 \pm 0.31$, and ZP $= -1.34 \pm 0.10$ for us. From their ZP ($H_0 = 70$ km s^{-1} Mpc^{-1}) we derive $M_I = -18.00 \pm 0.07$ mag ($M_i = -17.12 \pm 0.15$ mag for us). When the authors restrict the sample to objects in the Hubble flow, they end up with 20 SNe and a dispersion of 0.30 mag. If we perform the same cut, we find a dispersion of 0.29 for 24 SNe. We obtain consistent dispersion for both samples using similar filters. Note that reducing our sample to slow decliners alone ($s_2 \leqslant 1.5$, the classical SNe IIP in other studies) in the Hubble flow does not improve the dispersion. As mentioned in Section 5.3, the difference in dispersion between Olivares et al. (2010) and our study can be due, among other things, to the difference in epoch used, or that we calculate a power law for each SN for the velocity.

With respect to the NIR filters, Maguire et al. (2010) suggested that it may be possible to reduce the scatter in the Hubble diagram to 0.1–0.15 mag and this should then be confirmed with a larger sample and more SNe in the Hubble flow. The authors used 12 slow decliners but only 1 SN in the Hubble flow. Using the J band and the color $(V - J)$, they found a dispersion of 0.39 mag against 0.50 mag using the I band. From this drop in the NIR, the authors suggested that using this filter and more SNe in the Hubble flow could reduce the scatter from 0.25 to 0.3 mag (optical studies) to 0.1–0.15 mag. With the same filters used by Maguire et al. (2010), and using the Hubble flow sample, we find a dispersion of 0.28 mag with 24 SNe. This dispersion is 0.1 mag higher than that predicted by Maguire et al. (2010; 0.1–0.15 mag). To derive the fit parameters, the authors assumed an intrinsic color $(V - J)_0 = 1$ mag. They obtained $\alpha = 6.33 \pm 1.20$ and an absolute magnitude $M_J = -18.06 \pm 0.25$ mag ($H_0 = 70$ km s^{-1} Mpc^{-1}). If we use only the SNe with $cz_{\mathrm{CMB}} \geqslant 3000$ km s^{-1} (24 SNe), we find $\alpha = 4.64 \pm 0.64$ and ZP $= -2.44 \pm 0.18$, which corresponds to $M_J = -18.21 \pm 0.18$ mag assuming $H_0 = 70$ km s^{-1} Mpc^{-1}. If we include all SNe at any redshift, the sample goes up to 34 SNe and the dispersion is 0.31 mag. From all SNe we derive $\alpha = 4.87 \pm 0.52$ and ZP $= -2.44 \pm 0.20$ which corresponds to $M_J = -18.21 \pm 0.20$. To conclude, the Hubble diagram derived from the CSP sample using the SCM is consistent and somewhat better with those found in the literature.

More recently, Rodríguez et al. (2014) proposed another method to derive a Hubble diagram from SNe II. The PMM corresponds to the generalization of the SCM, i.e., the distances are obtained using the SCM at different epochs and then averaged. Using the $(V - I)$ color and the filter V, the authors found an intrinsic scatter of 0.19 mag. Given that the intrinsic dispersion used by Rodríguez et al. (2014) is a different metric than that used by us (the rms dispersion), we computed the latter from their data, obtaining 0.24 mag for 24 SNe in the

Hubble flow. Using the V band and the $(V - i)$ color and doing an average over several epochs,, we found a dispersion of 0.28 mag which is similar to the value found from the SCM and comparable with the value derived by Rodríguez et al. (2014). From the Y band and $(V - i)$ color we find an identical dispersion of 0.29 mag.

6.4. Low Number Effects

In analyzing the Hubble diagram, the figure of merit is the rms and the holy grail is to obtain very low dispersion in the Hubble diagram (i.e., low distance errors). In our work, we show that in the Y band we can achieve a rms around 0.43–0.48 mag using the Hubble flow sample (30 SNe) and the entire sample (41 SNe), whereas using the golden sample (8 SNe) we obtain a dispersion of 0.18 mag. It is important to know if this decrease in rms is due to the fact that we used well studied SNe within the golden sample or if it is due to the low number of SNe. For this purpose we do a test using the Monte Carlo bootstrapping method.

From our Hubble flow sample, we remove randomly one SN and compute the dispersion. We do that for 30,000 simulations and the final rms corresponds to the median, and the errors to the standard deviation. Then after removing 1 SN, we remove randomly 2 SNe and again estimate the rms and the dispersion over 30,000 simulations. We repeat this process until we have only four SNe, i.e., we remove from one SN to (size available sample—four SNe). For each simulation, we compute a new model, i.e., new fit parameters (α, β, and ZP).

From this test we conclude that when the number of SNe is lower than 10–12 SNe the rms is very uncertain because the parameters (i.e., α, β, and ZP) start diverging (see the Appendix). This implies that the rms is driven by the reduced number of objects so it is difficult to conclude if the model for the golden sample is better because the rms is smaller or because it is due to a statistical effect.

6.5. Low R_V

As stated in Section 4.1, the β_{λ_i} color term is related to the total-to-selective extinction ratio if the color–magnitude relation is due to extrinsic factors (dust). In the literature, for the MW, R_V is known to vary from one line of sight to another, from values as low as 2.1 (Welty & Fowler 1992) to values as large as 5.6–5.8 (Cardelli et al. 1989; Fitzpatrick 1999; Draine 2003). In general for the MW, a value of 3.1 is used which corresponds to an average of the Galactic extinction curve for diffuse interstellar medium. Using the minimization of the Hubble diagram with a color term, in the past decade the SNe Ia community has derived lower R_V for host galaxy dust than for the MW. Indeed, they found R_V between 1.5 and 2.5 (Krisciunas et al. 2007; Elias-Rosa et al. 2008; Goobar 2008; Folatelli et al. 2010; Phillips et al. 2013; Burns et al. 2014). This trend was also seen more recently using SNe II (Poznanski et al. 2009; Olivares et al. 2010; Rodríguez et al. 2014). This could be due to unmodeled effects such as a dispersion in the intrinsic colors (e.g., Scolnic et al. 2014).

We follow previous work in using the minimization of the Hubble diagram to obtain constraints on R_V for host galaxy dust. Using the PCM, the Hubble flow sample, and the r band, we find β_r close to 0.98. Using a Cardelli et al. (1989) law, we can transform this value in the total-to-selective extinction ratio, and we obtain $R_V = 1.01^{+0.53}_{-0.41}$. Following the same
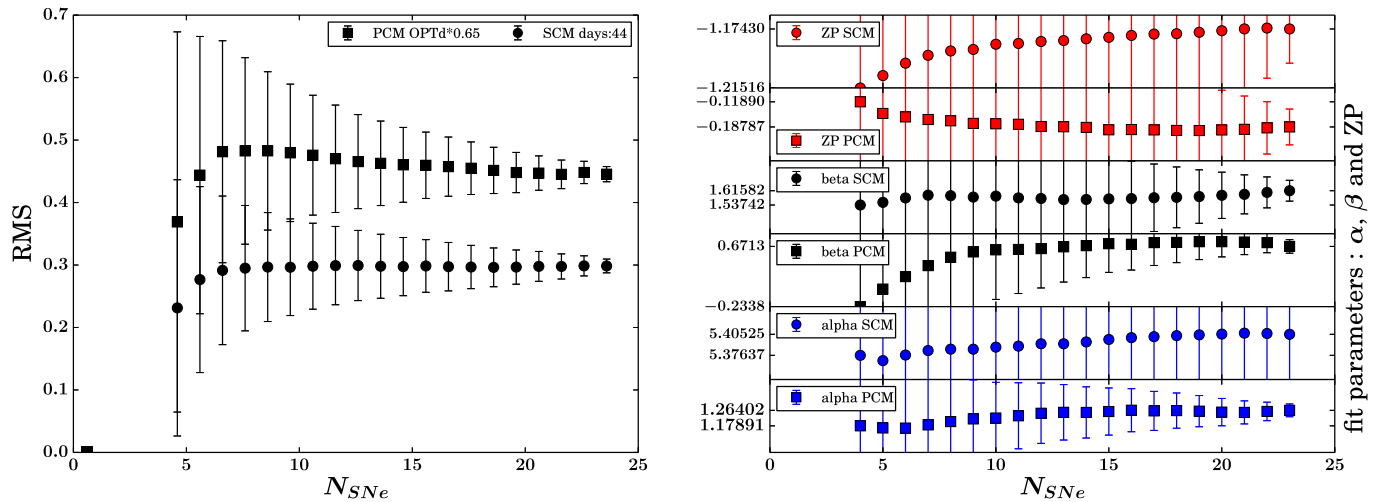
Figure 8. Left panel: we present the evolution of the rms vs. the number of SNe for one single epoch, OPTD*0.65 for the PCM and 65 days post-explosion for the SCM. We use the Y band and the $(V - i)$ color. The black squares represent the evolution for the PCM whereas the black circles are used for the SCM. Right panel: we present the evolution of our fit parameters $(\alpha, \beta, \text{and ZP})$ vs. the number of SNe. The black color represents the β, the red is for ZP, and the blue for α. The circles are used for the SCM and the squares for the PCM.

procedure but using the SCM, we also derive low R_V values, but consistent with those derived using the PCM.

At first sight, our analysis would suggest a significantly different nature of dust in our Galaxy and other spiral galaxies, as previously seen in the analysis of SNe Ia and SNe II. However, we caution that the low R_V values could reflect instead intrinsic magnitude–color for SNe II not properly modeled. To derive the R_V (or pseudo R_V) values, we assume that all the SNe II have the same intrinsic colors and same intrinsic color–luminosity relation; however, theoretical models with different masses and metallicity show different intrinsic colors (Dessart et al. 2013). Disentangling both effects would require to know the intrinsic colors of our SN sample. Indeed, with intrinsic color–luminosity corrections the β_{λ_1} color term could change and thus we will be able to derive an accurate R_V. In a forthcoming paper, we will address this issue through different dereddening techniques (T. de Jaeger 2016, in preparation) that we are currently investigating.

7. CONCLUSIONS

Using 38 SNe II in the Hubble flow, we develop a technique based solely on photometric data (PCM) to build a Hubble diagram based on SNe II. In summary:

1. Using PCM we find a dispersion of 0.44 mag using the r band and 0.43 mag with the Y band, thus using NIR filters the improvement is not so significant for the PCM.
2. The s_2 plays a useful role, allowing us to reduce the dispersion from 0.58 to 0.50 mag for the r band.
3. The color term does not have so much influence on the NIR filters because it is related to the host galaxy extinction.
4. We find very low (β) values (the color–magnitude coefficient). If β is purely extrinsic, it implies very low R_V values.
5. The Hubble diagram derived from the CSP sample using the SCM yields to a dispersion of 0.29 mag, somewhat better than those found in the literature and emphasizing the potential of SCM in cosmology.

It is also interesting to obtain more data and SNe for which the initial decline rate and the plateau are clearly visible to try to reduce this dispersion. The PCM is very promising, and more efforts must be done in this direction, i.e., trying to use only photometric parameters. In the coming era of large photometric wide-field surveys like LSST, having spectroscopy for every SNe will be impossible hence the PCM which is the first purely photometric method could be very useful.

APPENDIX

Figure 8 (left) presents the evolution of the rms versus the number of SNe for both methods (PCM and SCM) using the Y band. For both methods, after a constant median value the rms decreases when the number of SNe is lower than 10–12 SNe because the model starts diverging. Indeed, if we look at the Figure 8 on the right where the evolution of the fit parameters versus the number of SNe for one single epoch (OPTD*0.55) and the Y band are presented, we see that for the PCM, α, β,

and ZP change significantly when the number of SNe is around 12. The values start diverging for a number of SNe smaller than 12, so this implies that the rms is driven by the reduced number of objects and therefore it will be difficult to conclude between the fact that β and ZP are better because we have a better rms or because it is due to a statistical effect. Note that the figure does not present directly the value of the fit parameters but a fraction of the value, i.e., the value divided by the first value plus an offset corresponding to the first value.

REFERENCES

Anderson, J. P., Dessart, L., Gutierrez, C. P., et al. 2014a, MNRAS, 441, 671
Anderson, J. P., González-Gaitán, S., Hamuy, M., et al. 2014b, ApJ, 786, 67
Arcavi, I., Gal-Yam, A., Cenko, S. B., et al. 2012, ApJL, 756, L30
Barbon, R., Ciatti, F., & Rosino, L. 1979, A&A, 72, 287
Baron, E., Nugent, P. E., Branch, D., & Hauschildt, P. H. 2004, ApJL, 616, L91
Benedict, G. F., McArthur, B. E., Feast, M. W., et al. 2007, AJ, 133, 1810
Bennett, C. L., Hill, R. S., Hinshaw, G., et al. 2003, ApJS, 148, 1
Bersten, M. C., Benvenuto, O. G., Folatelli, G., et al. 2014, AJ, 148, 68
Bessell, M., & Murphy, S. 2012, PASP, 124, 140
Betoule, M., Kessler, R., Guy, J., et al. 2014, A&A, 568, A22
Blake, C., & Glazebrook, K. 2003, ApJ, 594, 665
Blondin, S., Mandel, K. S., & Kirshner, R. P. 2011, A&A, 526, A81
Burns, C. R., Stritzinger, M., Phillips, M. M., et al. 2014, ApJ, 789, 32
Cardelli, J. A., Clayton, G. C., & Mathis, J. S. 1989, ApJ, 345, 245
Chevalier, R. A. 1976, ApJ, 207, 872
Chevalier, R. A. 1981, ApJ, 251, 259
Chugai, N. N., & Danziger, I. J. 1994, MNRAS, 268, 173
Contreras, C., Hamuy, M., Phillips, M. M., et al. 2010, AJ, 139, 519
D'Andrea, C. B., Sako, M., Dilday, B., et al. 2010, ApJ, 708, 661
de Jaeger, T., Anderson, J. P., Pignata, G., et al. 2015, ApJ, 807, 63
Dessart, L., Blondin, S., Brown, P. J., et al. 2008, ApJ, 675, 644
Dessart, L., & Hillier, D. J. 2005, A&A, 439, 671
Dessart, L., & Hillier, D. J. 2006, A&A, 447, 691
Dessart, L., Hillier, D. J., Livne, E., et al. 2011, MNRAS, 414, 2985
Dessart, L., Hillier, D. J., Waldman, R., & Livne, E. 2013, MNRAS, 433, 1745
Draine, B. T. 2003, ARA&A, 41, 241
Eastman, R. G., Schmidt, B. P., & Kirshner, R. 1996, ApJ, 466, 911
Elias-Rosa, N., Benetti, S., Turatto, M., et al. 2008, MNRAS, 384, 107
Elias-Rosa, N., Van Dyk, S. D., Li, W., et al. 2010, ApJL, 714, L254
Elias-Rosa, N., Van Dyk, S. D., Li, W., et al. 2011, ApJ, 742, 6
Emilio Enriquez, J., Leonard, D. C., Poznanski, D., et al. 2011, BAAS, 43, 33721
Falk, S. W., & Arnett, W. D. 1977, ApJS, 33, 515
Faran, T., Poznanski, D., Filippenko, A. V., et al. 2014a, MNRAS, 445, 554
Faran, T., Poznanski, D., Filippenko, A. V., et al. 2014b, MNRAS, 442, 844
Filippenko, A. V. 1997, ARA&A, 35, 309
Filippenko, A. V., Matheson, T., & Ho, L. C. 1993, ApJL, 415, L103
Fitzpatrick, E. L. 1999, PASP, 111, 63
Fixsen, D. J., Cheng, E. S., Gales, J. M., et al. 1996, ApJ, 473, 576
Folatelli, G., Morrell, N., Phillips, M. M., et al. 2013, ApJ, 773, 53
Folatelli, G., Phillips, M. M., Burns, C. R., et al. 2010, AJ, 139, 120
Fransson, C. 1982, A&A, 111, 140
Goobar, A. 2008, ApJL, 686, L103
Grassberg, E. K., Imshennik, V. S., & Nadyozhin, D. K. 1971, Ap&SS, 10, 28
Gutiérrez, C. P., Anderson, J. P., Hamuy, M., et al. 2014, ApJL, 786, L15

Hamuy, M., Folatelli, G., Morrell, N. I., et al. 2006, PASP, 118, 2
Hamuy, M., Phillips, M. M., Suntzeff, N. B., et al. 1996, AJ, 112, 2391
Hamuy, M., & Pinto, P. A. 2002, ApJL, 566, L63
Hamuy, M., Pinto, P. A., Maza, J., et al. 2001, ApJ, 558, 615
Hamuy, M. A. 2001, PhD thesis, Univ. Arizona
Hsiao, E. Y., Conley, A., Howell, D. A., et al. 2007, ApJ, 663, 1187
Ivezic, Z., Tyson, J. A., Axelrod, T., et al. 2009, BAAS, 41, 46003
Jaffe, A. H., Ade, P. A., Balbi, A., et al. 2001, PhRvL, 86, 3475
Jones, M. I., Hamuy, M., Lira, P., et al. 2009, ApJ, 696, 1176
Kankare, E., Ergon, M., Bufano, F., et al. 2012, MNRAS, 424, 855
Kasen, D., & Woosley, S. E. 2009, ApJ, 703, 2205
Kirshner, R. P., & Kwan, J. 1974, ApJ, 193, 27
Krisciunas, K., Garnavich, P. M., Stanishev, V., et al. 2007, AJ, 133, 58
Kuncarayakti, H., Maeda, K., Bersten, M. C., et al. 2015, A&A, 579, 95
Landolt, A. U. 1992, AJ, 104, 340
Leavitt, H. S. 1908, AnHar, 60, 87
Leonard, D. C., Kanbur, S. M., Ngeow, C. C., & Tanvir, N. R. 2003, ApJ, 594, 247
Li, W., Leaman, J., Chornock, R., et al. 2011, MNRAS, 412, 1441
Lien, A. Y., Fields, B. D., Beacom, J. F., Chakraborty, N., & Kemball, A. 2011, BAAS, 43, 33728
Maguire, K., Kotak, R., Smartt, S. J., et al. 2010, MNRAS, 403, L11
Massey, P., Morrell, N. I., Neugent, K. F., et al. 2012, ApJ, 748, 96
Minkowski, R. 1941, PASP, 53, 224
Nugent, P., Sullivan, M., Ellis, R., et al. 2006, ApJ, 645, 841
Olivares, F., Hamuy, M., Pignata, G., et al. 2010, ApJ, 715, 833
Perlmutter, S., Aldering, G., Goldhaber, G., et al. 1999, ApJ, 517, 565
Persson, S. E., Madore, B. F., Krzemiński, W., et al. 2004, AJ, 128, 2239
Phillips, M. M. 1993, ApJL, 413, L105
Phillips, M. M., Simon, J. D., Morrell, N., et al. 2013, ApJ, 779, 38
Planck Collaboration Ade, P. A. R., Aghanim, N., et al. 2014, A&A, 571, 16
Popov, D. V. 1993, ApJ, 414, 712
Poznanski, D., Butler, N., Filippenko, A. V., et al. 2009, ApJ, 694, 1067
Richardson, D., Branch, D., Casebeer, D., et al. 2002, AJ, 123, 745
Riess, A. G., Filippenko, A. V., Challis, P., et al. 1998, AJ, 116, 1009
Riess, A. G., Macri, L., Casertano, S., et al. 2011, ApJ, 730, 119
Riess, A. G., Press, W. H., & Kirshner, R. P. 1996, ApJ, 473, 88
Rodríguez, Ó., Clocchiatti, A., & Hamuy, M. 2014, AJ, 148, 107
Sanders, N. E., Soderberg, A. M., Gezari, S., et al. 2015, ApJ, 799, 208
Schlafly, E. F., & Finkbeiner, D. P. 2011, ApJ, 737, 103
Schlegel, E. M. 1990, MNRAS, 244, 269
Schmidt, B. P., Kirshner, R. P., Eastman, R. G., et al. 1994, ApJ, 432, 42
Schmidt, B. P., Suntzeff, N. B., Phillips, M. M., et al. 1998, ApJ, 507, 46
Scolnic, D., Rest, A., Riess, A., et al. 2014, ApJ, 795, 45
Seo, H.-J., & Eisenstein, D. J. 2003, ApJ, 598, 720
Smartt, S. J. 2009, ARA&A, 47, 63
Smartt, S. J., Eldridge, J. J., Crockett, R. M., & Maund, J. R. 2009, MNRAS, 395, 1409
Smith, J. A., Tucker, D. L., Kent, S., et al. 2002, AJ, 123, 2121
Spergel, D. N., Bean, R., Doré, O., et al. 2007, ApJS, 170, 377
Stritzinger, M. D., Phillips, M. M., Boldt, L. N., et al. 2011, AJ, 142, 156
Taddia, F., Stritzinger, M. D., Sollerman, J., et al. 2012, A&A, 537, A140
Takáts, K., & Vinkó, J. 2012, MNRAS, 419, 2783
Taylor, M., Cinabro, D., Dilday, B., et al. 2014, ApJ, 792, 135
Tripp, R. 1998, A&A, 331, 815
Van Dyk, S. D., Li, W., & Filippenko, A. V. 2003, PASP, 115, 1289
Van Dyk, S. D., Peng, C. Y., King, J. Y., et al. 2000, PASP, 112, 1532
Welty, D. E., & Fowler, J. R. 1992, ApJ, 393, 193
Woosley, S. E., Pinto, P. A., Martin, P. G., & Weaver, T. A. 1987, ApJ, 318, 664